J Nanostruct 12(1): 99-112, Winter 2022

RESEARCH PAPER

Green Modification of Iron Oxide Nanoparticles with Achillea wilhelmsii and Investigation of Their Performance for Methylene Blue Adsorption

*Zahra Pourmanouchehri [1,2], Azam Chahardoli [2,3], Farshad Qalekhani [1,2], Hossein Derakhshankhah [2], Yalda Shokoohinia [1,4], Ali Fattahi [1,2] *, and Alireza Khoshroo [1,2] **

[1] Department of Pharmaceutics, Faculty of Pharmacy, Kermanshah University of Medical Sciences, Kermanshah, Iran

[2] Pharmaceutical Sciences Research Center, Kermanshah University of Medical Sciences, Kermanshah, Iran

[3] Department of Biology, Faculty of Science, Razi University, Kermanshah, Iran

[4] Ric Scalzo Botanical Research Institute, Southwest College of Naturopathic Medicine, Tempe, AZ, USA

ARTICLE INFO

Article History:
Received 02 September 2021
Accepted 15 December 2021
Published 01 January 2022

Keywords:
Adsorption
A. wilhelmsii C.koch
Fe_3O_4 NPs
Green synthesis
Methylene blue

ABSTRACT

Biosynthesis of nanoparticles (NPs) by plant extracts as a one-pot, cost-effective and rapid method has attracted the great attention due to the controllable properties of nanoparticles. Herein, for the first time we report a method for synthesis of a polyphenol modified magnetically separable Fe_3O_4 NPs by aqueous extract of Achillea wilhelmsii C. Koch (Aw) leaves as a natural capping and reducing agent for water remediation purposes. Aw is the native plant of Iran with high amount of polyphenol compound that its aqueous leaf extract offers several advantages, including modification of structures and improving the physical and chemical properties of the Fe_3O_4. The prepared nanoparticles possessed great magnetism (~60), pure crystalline structure, and high adsorption capacity toward cationic dye like methylene blue (MB) (~8 mg/g). The Aw-Fe_3O_4 nanoparticles displayed pH-responsive behavior. With an increase in pH value, the phenolic compounds were deprotonated and revealed enhanced electrostatic interactions with high MB removal efficiency (73%). The intra-particle diffusion and pseudo-second-order kinetic model were suitable to illustrate the adsorption processes of MB. Moreover, the obtained nanoparticles showed efficient reusability after three cycles. Altogether, the finding of this study demonstrates that Aw-Fe_3O_4 NPs can be considered as a suitable adsorbent to purify dye wastewater.

How to cite this article
Pourmanouchehri Z, Chahardoli A, Qalekhani F, Derakhshankhah H, Shokoohinia Y, Fattahi A, Khoshroo A. Green Modification of Iron Oxide Nanoparticles with Achillea wilhelmsii and Investigation of Their Performance for Methylene Blue Adsorption. J Nanostruct, 2022; 12(1):99-112. DOI: 10.22052/JNS.2022.01.010

INTRODUCTION

Due to the development of industries relied on textile, leather, plastic, and furniture, environmental issues are growing, and the outlook for the use of novel materials for environmental remediation is still a challenge [1]. Among contaminants, organic dyes, specifically in the textile industry, are considered a significant threat because of the huge proportion of waste that enters the water supply [2–4]. Synthetic dyes

* Corresponding Author Email: khoshroo.a.r@gmail.com
alifattahi@kums.ac.ir

with carcinogenic and mutagenic properties cause harmful effects on human health, e.g., vomiting, eye irritation, skin dermatitis, respiratory diseases, nausea, cyanosis, and tissue necrosis [5,6]. Thus, efforts were made to purify the aquatic ecosystem contaminated with such dyes. Diverse methods have been applied for the removal of dyes from wastewater, including adsorption [7], electrocoagulation [8], dissolved air floatation [9], and reduction [10]. Amongst these methods, dye adsorption has been widely investigated due to its high efficiency, simplicity, and economic benefits. For this purpose, a wide variety of materials such as alumina, silica gel, zeolites, and activated carbons were introduced as dye adsorbents, but their shortcoming in separation from water limits their application [11].

Superparamagnetic iron oxide nanoparticles have aroused great attention in several fields like catalysis, sensor, cancer therapy, targeted drug delivery, and magnetic resonance imaging [12–14]. The utilizing of iron oxides and their composite for dye adsorption has also been attempted [15,16]. The main reason for such an impact of Fe_3O_4 NPs is their unique physical and chemical properties, e.g., superparamagnetic and high surface-to-volume ratios [17,18]. Different methods (hydrothermal/solvothermal hydrolysis, sonochemical, micro-emulsion, electrochemical, laser pyrolysis, surfactant mediated/template synthesis, sol-gel, and co-precipitation) have been widely used for the synthesis of Fe_3O_4 MNPs [19]. For example in the literature, the $NaBH_4$, anhydrous sodium sulfite, ethylene glycol, N_2H_4 and etc., have been used as the reducing agent or solvent for the synthesis of Fe_3O_4 particles [20–25]. For these synthetic procedures, toxic, highly reactive, or non-environmentally and, biologically friendly solvents/chemicals are used [26]. Lately, these methods have been modified and developed in terms of efficiency, cost optimization, environmentally friendly, and time required to generate nanoparticles [27]. In particular, with the development of green technology, attention has shifted towards the biological synthesis of metallic nanoparticles, though few reports have been available on the green synthesis of magnetic Fe_3O_4 NPs [28–31]. In the green method, natural biopolymers, secondary metabolites, and compounds are used for synthesis of Fe_3O_4 NPs due to abundant availability, low cost, strong metal capping affinity, biodegradability, green solvent and reducing agents [32,33]. Applying this green route, promote the application of magnetic

Fig. 1. Dried Achillea wilhelmsii C. Koch plant (May 2017).

Fe_3O_4 NPs in catalysis, magnetic resonance imaging, biosensors, drug delivery, cancel cell amelioration, and etc. [34]. Fe_3O_4 NPs have been synthesized using plant extracts such as green tea, pomegranate leaves, silky hairs of corn, root extract of Chromolaena odorata [35,36]. Since synthesis and modification of Fe_3O_4 NPs by aqueous extract of plant materials no longer is known as a novel technique, difference in adsorption and catalytic activity of these nanoparticles from various plant sources made it attractive for screening study of herbal mediated Fe_3O_4 NPs. Furthermore, Fe_3O_4 NPs attracted the great attention in the color removal application, due to their magnetic properties which accelerate the process of catalyst or adsorbent collection [37]. Here, for the first time we use *A. wilhelmsii C. Koch* extract to synthesis Aw-Fe_3O_4 NPs as a reducing and stabilizing agent. The Achillea genus (Asteraceae) is a medicinal herb with more than 100 species native to Western Asia, North America, and Europe [38]. Nineteen species of this genus are widely found in different regions of Iran, where *A. wilhelmsii* is the dominant species of this genus. *A. wilhelmsii C.Koch* (Fig. 1) is rich in flavonoids, sesquiterpenes, borneol, cineol, thujene, α and, β pinene, camphor, caryophyllene, alkaloids (achilleine), rutin, and monoterpenoids [39,40]. The existence of specific polyphenol compounds in the extract is related to essential factors in extraction, including the type of solvent, extraction temperature, and solvent volume [41–43]. *A. wilhelmsii* has shown many biological activities such as antimicrobial, antiacid, antifungal, and antioxidant properties [44,45]. Further, the synthesized Aw-Fe_3O_4 NPs were investigated for their application in the adsorption of MB as a cationic organic dye by spectroscopy, microscopy, and analytic techniques. The effects of pH and adsorbent dosage on MB removal by nanoparticles were studied. To discuss the adsorption mechanism, adsorption properties containing kinetics, and reusability were also analyzed.

MATERIALS AND METHODS

Iron (II) chloride tetrahydrate ($FeCl_2.4H_2O$ ≥ 99 %), iron (III) chloride hexahydrate ($FeCl_3.6H_2O$, 97 %), ammonia (NH_3, 25%), hydrochloric acid (HCl), sodium hydroxide (NaOH), Gallic acid, 1,1-Diphenyl-2-picryl-hydrazyl (DPPH), and quercetin were purchased from Sigma-Aldrich. These chemicals were used without further purification. Achillea wilhelmsii C. Koch was collected in summer 2018 from Kermanshah Mountains, Kermanshah, Iran, at an altitude of 1600 m. Samples for identification were made by Dr. Masoumi (Herbarium of Research Center of Agriculture College, Razi University, Kermanshah, Iran). Herbarium vouchers were kept at the Department of Pharmacognosy, Kermanshah University of Medical Sciences, Kermanshah, Iran, under the voucher 2729.

Preparation of aqueous extracts

The Achillea wilhelmsii C. Koch leaves were soaked and washed to remove dirt and foreign particles via deionized water. The leaves were dried and powdered via an electric grinder. Finally, 15 g of dried powder was added to 100 mL of distilled water and boiled for 15 min with continuous stirring. The solutions were cooled at room temperature, filtered, centrifuged with universal 320-centrifuge, and stored in a glass bottle at −20 °C for further synthesis of Aw-Fe3O4 NPs [37].

Synthesis of magnetic Fe_3O_4 NPs

Aw- Fe_3O_4 NPs were synthesized using the green technology method. For the synthesis, both iron ions were taken as precursor compounds, while the Achillea wilhelmsii C. Koch extracts were used as a capping agent. Initially, 0.54 g of $FeCl_3$ and 0.2 g of $FeCl_2$ were dissolved in 8 mL of distilled water. The solution was then heated at 30 °C with continuous stirring. After 15 min of constant stirring, 3 mL of the Achillea wilhelmsii C. Koch extracts were added to the mixture solutions drop by drop and temperature adjusted at 80°C. About 1 mL of 25% ammonia was added at a rate of 0.5 mL/min to permit the formation of uniform magnetite particles. After observing the black color in the solution, the reaction mixtures were allowed to cool at room temperature, and the Aw-Fe_3O_4 NPs were separated using an external magnet. The NPs were then washed with distilled water and ethanol several times. The pellets were dried in an oven at 60 °C and stored at room temperature for further characterization [37]. The chemical Fe_3O_4 NPs (C-Fe_3O_4 NPs) were synthesized by co-precipitation method. Briefly, 0.54 g of $FeCl_3$ and 0.2 g of $FeCl_2$ were added to 10 mL deionized water and stir for 10 min. After that 25% ammonia solution was added drop wise until

the pH reach to 11. Finally, after 1 h stirring, the NPs collected with external magnet and washed several time with water and twice with ethanol and left to dry in room temperature.

Determination of total phenolic contents

The Folin-Ciocalteu method was used to determine the total phenolics of aqueous extract and Aw-Fe_3O_4 NPs [46]. First, 1 mL of the Folin-Ciocalteu reagent (0.2N) was added to 200 µL of the different concentrations of the sample solution, and the contents of the tube were mixed thoroughly. After 10 min, 0.8 mL Na_2CO_3 (7.5 %) was added, and the mixture was allowed to stand for 2 h. The distilled water with Folin-Ciocalteu and Na_2CO_3 was used as a blank. The absorbance was measured at 765 nm. The experiment was repeated in triplicate using an equation gained from the standard calibration curve of gallic acid. The total phenolic content was explained as mg of gallic acid equivalent (GAE) per gram of dried weight of the extract (DE).

Determination of total flavonoid contents

The calculation of the total flavonoid content of aqueous extract and Aw-Fe_3O_4 NPs was performed by the colorimetric method of aluminum chloride with some modification [47]. 500 µL of the methanolic solution of the sample was mixed with 500 µL of aluminum chloride (10% w/v). The mixture was retained at room temperature for 1h. The absorbance was determined at 415 nm by a spectrophotometer, and methanol was used as blank. The experiment was repeated in triplicate, and the total flavonoid content was explained using an equation gained from the calibration curve of quercetin as mg of quercetin per gram of dried weight of the extract (DE).

Determination of radicals scavenging activity (DPPH)

The free radical scavenging activity of aqueous extract and Aw-Fe_3O_4 NPs was determined based on the method used in our previous study [48]. Briefly, 0.5 mL of sample solution with varying concentrations was added to 0.5 mL of the DPPH radical solution in methanol (0.1 mM). After shaking vigorously, it was incubated in the dark at room temperature for 30 min. All experiments were conducted in triplicate, and the DPPH radical inhibition was measured at 517 nm using a UV–Vis spectrophotometer. 500 µL methanol with a 500 µL DPPH solution was used as a control. The optical density was recorded, and the percentage of inhibition was calculated by the formula given below as means ± SD.

$$\text{means} \pm \text{SD\% } inhibition = \frac{A_{control} - A_{sample}}{A_{control}} \times 100 \qquad (1)$$

Removal tests of MB

The methylene blue adsorption study was experimentally performed by adding adsorbent to the dye solution at ambient conditions. For absorption kinetics, a series of 50 mL flask containing different amounts of Aw-Fe_3O_4 NPs (10, 50, 100, 150 mg) and 35 mL of MB solution at a concentration of 30 ppm was prepared. The 0.1 M HCl or NaOH solution was used to adjust MB pH before adding Aw-Fe_3O_4 NPs. The mixture was then stirred at 500 rpm for 2 h in a water bath shaker. At certain time intervals, the Aw-Fe_3O_4 NPs were isolated by an external magnet, and the MB concentration was analyzed through UV–Vis spectroscopy.

The decolorization of MB, (dye adsorption capacity per unit of adsorbent at given time t, (q_t, mg/g), and at equilibrium (q_e)) were calculated using Eq. 2, 3, and 4, respectively:

$$Decolourization\ (\%) = \frac{Abs_0 - Abs_t}{Abs_0} \times 100 \qquad (2)$$

$$q_t = \frac{(C_0 - C_t)V}{m_a} \qquad (3)$$

$$q_e = \frac{(C_0 - C_e)V}{m_a} \qquad (4)$$

Where Abs_0 is the MB absorbance at time=0, and Abs_t is the MB absorbance at a given time (min); C_o is the initial concentration of MB (mg/L); C_t, is the concentration of MB (mg/L) at time t; C_e is the equilibrium concentration of MB (mg/L); V is a volume of the dye solution (L) and m_a is the weight of Aw-Fe_3O_4 NPs (g).

Reusability of the Aw-Fe_3O_4 NPs

A batch experiment was done for three cycles of MB dye sorption and desorption process. Desorption was done in 100 mL round bottom flasks containing 100 mg of Aw-Fe_3O_4 NPs for 2 h at room temperature using 50 mL of HCl (0.5 M) solution as eluent. After isolating with an external magnet and washing with distilled water, particles were dried at 60 °C, and reuse in the next round

reaction.

Characterization

The prepared Aw-Fe_3O_4 NPs were characterized by Irprestige-2, Shimadzu- FT-IR spectroscopy, mini 1240 Shimadzu- UV–Vis spectroscopy, Bruker AXSD8 X-ray powder diffractometer (XRD), the Nano ZS Zetasizer (Malvern Instruments Ltd., Worcestershire, UK), Belsorp mini II, Japan to measure nitrogen adsorption-desorption, Germany Zeiss LEO 906, 80 kV transmission electron microscope (TEM), and Image J.

RESULTS AND DISCUSSION

Recently, a wide range of plant extracts was used as reducing and capping agents in the synthesis of NPs [47,49]. Studies show that the secondary metabolites of leaf extracts are very desirable for the green synthesis of stable nanoparticles; they not only act as natural reducing metal ion agents but also are considered as capping agents and preventing oxygen penetration into the nanoparticle network [50,51]. The phenolic and flavonoid content and antioxidant activity of aqueous extract of *A. wilhelmsii C. Koch* can provide a relative estimate of the presence of some compounds in the extract. The TPC and TFC content in the aqueous extracts were calculated using gallic acid (GA), and quercetin (QE) standard curves as 159.81 ± 4.09 mg GAE/g DE and 103.57 ± 0.85 mg QE/g DE, respectively. This amount is much higher than the calculated TPC (55.77±2.94 GAE mg/g DE) and TFC (11.28±1.05 QE mg/g DE) from hydroethanolic extract of *A. wilhelmsii C. Koch* obtained by Khazneh et al.[40], which indicates the effect of infusing on the extraction of phenolic compounds from this plant. The scavenging ability of the samples is summarized in Table S1. Results indicated that the concentration-dependent activity profile of the extract and the scavenging activities of the extracts increased with an increasing phenolic and flavonoid content. Results of the DPPH assay illustrated that A·wilhelmsii C. Koch extract had a moderate antioxidant activity that conforming to the data recently reported with different extraction solvents [52,53].

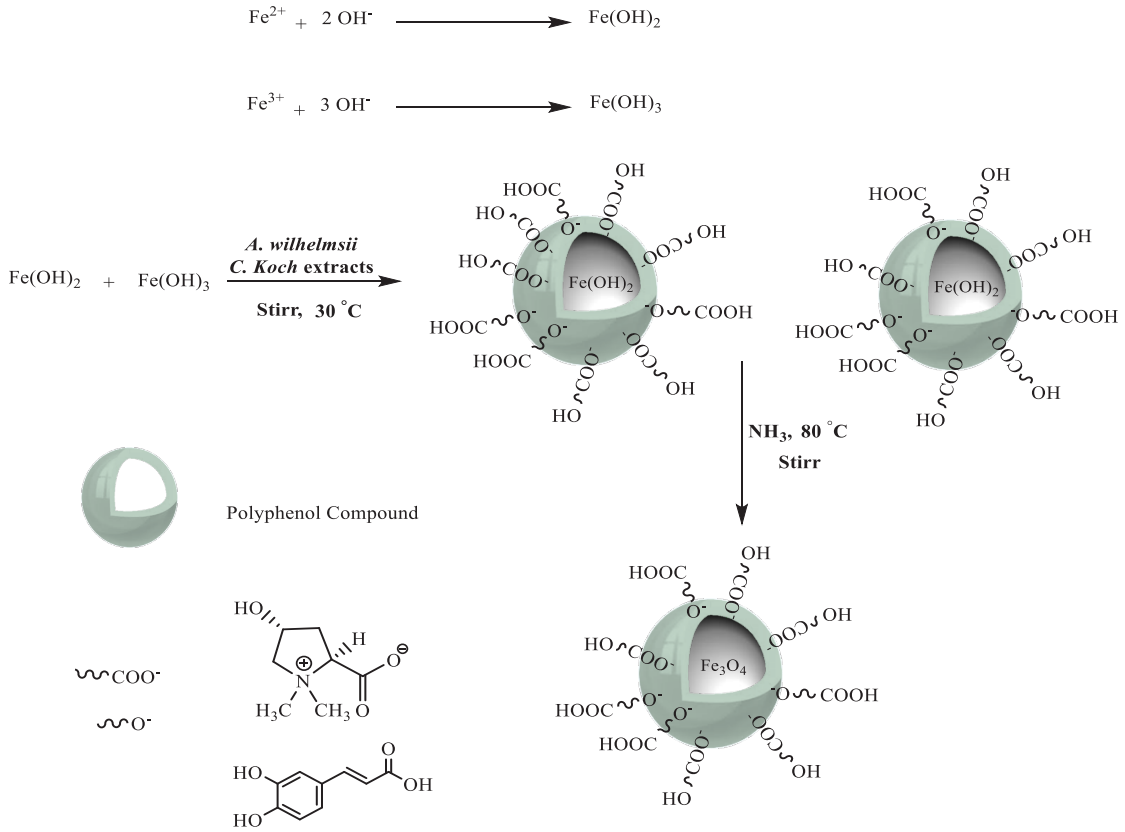

Fig. 2. Possible mechanism for synthesis of Aw-Fe_3O_4 NPs.

Synthesis mechanism of Aw-Fe_3O_4 NPs

Based on the contributing mechanism using Fe^{2+} and Fe^{3+} salts in alkaline conditions, Fe^{3+} and Fe^{2+} salts were hydrolyzed and dehydrated simultaneously during magnetite nanoparticle nucleation [54]. By adding aqueous *A. wilhelmsii C. Koch* extract, the hydroxyl and carboxyl group of polyphenol compounds present in the *A. wilhelmsii* extract, such as achilleine, caffeic acid, and ferulic acid, chelates ferric and ferrous hydroxide, and the color of the mixture immediately turned from the yellow to greenish-black. Based on the acidic pH of the solution after the addition of extract (pH=4.6), we expect ferrihydrite precipitate was formed by hydrolysis of $Fe(OH)_3$ at room temperature [55]. Subsequent charging ammonia into the solution and increasing the temperature leads to forming intermediate Fe^{2+}-ferrihydrite complexes by incorporation of Fe^{2+} into ferrihydrite [54,56,57]. Ultimately, spinal magnetite nanoparticle structures were synthesized. A more detailed description of the synthesis and in situ modification of Aw-Fe_3O_4 nanoparticles is given in Fig. 2.

Characterization of Aw-Fe_3O_4 NPs

UV-Vis spectroscopy was performed to confirm the formation of Aw-Fe_3O_4 NPs. The UV-Vis spectra of $FeCl_3$, *A. wilhelmsii C. Koch*, and Aw-Fe_3O_4 NPs were shown in Fig. 3a. The Aw-Fe_3O_4 NPs showed continuous absorption in the visible range between 200 to 600 nm. The UV–Vis spectrum of the *A. wilhelmsii C. Koch* aqueous extract shows two major absorption peaks; at 331 nm, associated to the band I corresponding to the transition localized within the B ring of cinnamoyl system and at 272 nm associated with band II for absorption involving the A ring benzoyl system of flavonoids compounds. This result reflects the presence of a high concentration of phytochemicals like flavonoids with conjugated double bonds [58,59]. The UV–vis spectrum of the $FeCl_3.6H_2O$ solution in water reveals an absorbance peak at 299 nm, which indicates transition metal elements in the filled and unfilled d-orbitals compounded by influences from other external factors. In the case of Fe_3O_4, disappearing Fe^{3+} peaks at 299 nm and emerge continuous absorption in the visible range

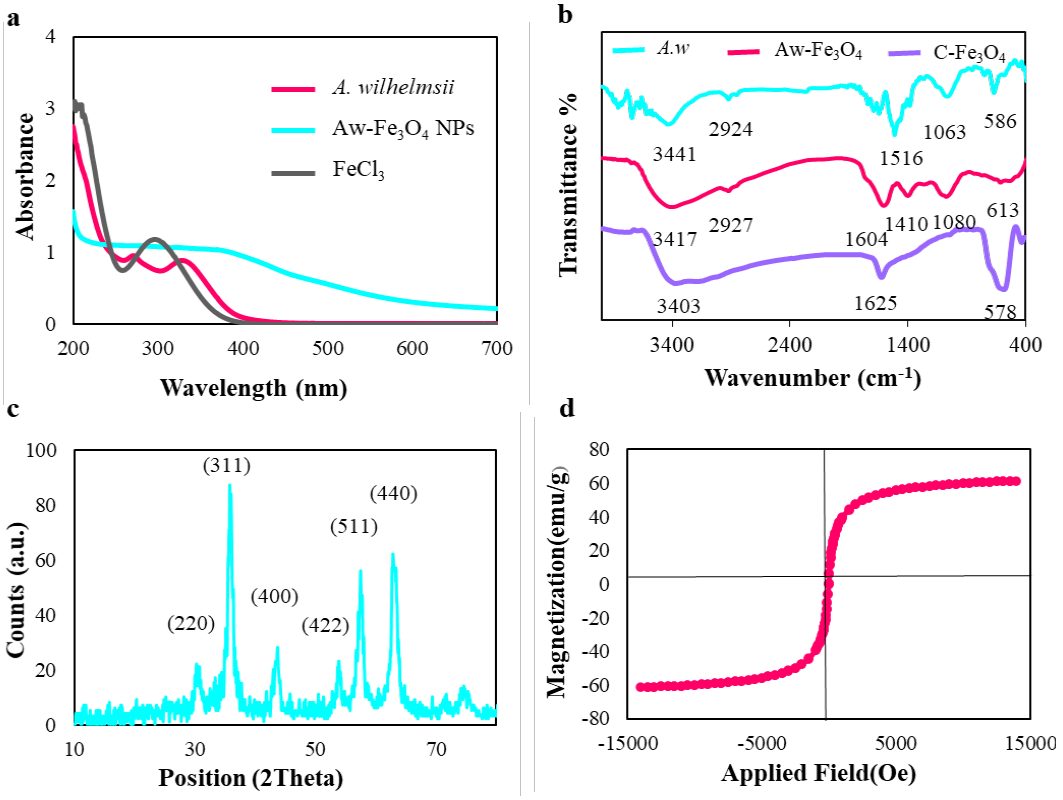

Fig. 3. (a) UV–vis spectra of the aqueous extract of A. wilhelmsii, $FeCl_3.6H_2O$ solution in water, and green synthesized Aw-Fe_3O_4 NPs; (b) FT-IR spectra of A. wilhelmsii aqueous extract, C- Fe_3O_4 NPs, and Aw-Fe_3O_4 NPs; (c) XRD patterns and (d) Room temperatures VSM curve of Aw-Fe_3O_4 NPs.

of 200 to 400 nm shows the new cation of Fe was formed [60].

Fig. 3b shows the FT-IR spectra of the freeze-dried *A. wilhelmsii C. Koch* aqueous extract, C-Fe_3O_4, and the Aw-Fe_3O_4 NPs. The spectrum of *A. wilhelmsii C. Koch* aqueous extract showed the characteristic peaks of both heterocyclic compounds like alkaloids or flavones and amide I bonds derived from the proteins, including 3417 cm^{-1} (OH stretching), 2927 cm^{-1} (symmetric CH_2 stretching), 1604 cm^{-1} (N-H deformation of amide I), 1410 cm^{-1} (C-N stretching), 1080 cm^{-1} (C-O stretching), 613 cm^{-1} (C=O out of plane bending) and 540 cm^{-1} (COO rocking) [61–63]. In the IR spectrum of C-Fe_3O_4 NPs, the peak at 578, 1625, and 3403 cm^{-1} attributed to the Fe-O vibrations, bending vibrations of OH, and stretching OH vibration of magnetite. For green synthesized Aw-Fe_3O_4 NPs, intensities located at 586 and 462 cm^{-1} are ascribed to the Fe-O bond in the tetrahedral and octahedral structure. The peaks appearing at 3441 and 2924 cm^{-1} are attributed to the OH stretching vibration and C-H stretching vibrations in the CH_2 groups, respectively. The bands at 1516 and 1388 cm^{-1} are related to C–C stretching vibration in ring of the aromatic compounds and COO symmetric stretching, respectively. The band observed at 1068 cm^{-1} can be related to the C-O stretching of carboxylic acids groups presents in the flavonoids, which agree with UV–vis spectroscopy results [5].

The phase purity and crystalline structure of the Aw-Fe_3O_4 NPs were confirmed by XRD analysis (Fig. 3c). The main diffraction peaks appear at 2θ = 30.4°, 35.8°, 43.4°, 53.8°, 57.4°, and 63.0° corresponding to the reflection planes of (220), (311), (400), (422), (511), and (440) of magnetite, respectively (JCPDS, PDF Card No.: 75-0449) [64]. The observed diffraction pattern indicates the highly crystalline structure of Aw-Fe_3O_4 NPs, which can be assigned as an inverse-spinel structure. The average crystallite size of the NPs calculated from the (311) facet using the Debye-Scherrer equation (Eq. (5)) was found to be 22 nm [65].

$$D = \frac{K\lambda}{\beta cos\theta} \quad (5)$$

Where K = 0.89, λ = 0.154 nm, β is the full width at half maximum, and θ is the Bragg's angle. With the aim of this fact that the separation of adsorbents from solution requires appropriate magnetic strength, the vibrating sample magnetometer (VSM) study was performed.

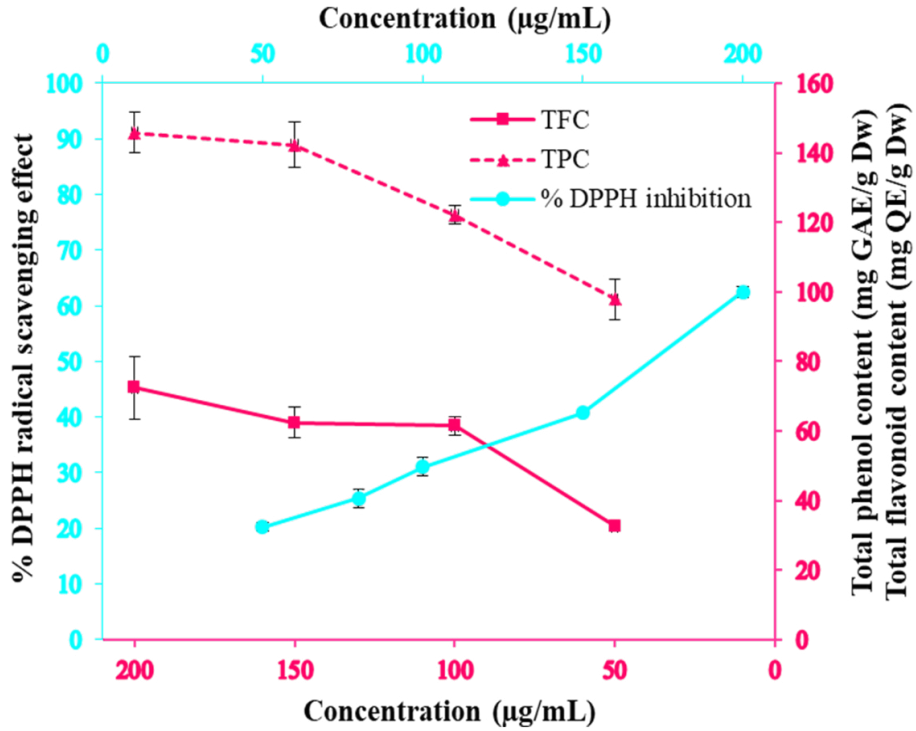

Fig. 4. Total phenolic content (mg GAE/g dried weight), total flavonoid content (mg QE/g dried weight), and DPPH inhibition (%) of Aw-Fe_3O_4 NPs.

As illustrated in Fig. 3d, the measured specific saturation magnetization value was 61.27 emu/g, which indicated the superparamagnetic nature of the Aw-Fe_3O_4 NPs. This value conforming to other reported Ms values for bio-functionalized superparamagnetic Fe_3O_4 nanoparticles [35,66].

To further investigate the capping of organic compounds on the surface of nanoparticles, the total phenolic contents (TPC), total flavonoids (TFC), and DPPH inhibition (%) of Aw-Fe_3O_4 NPs were determined (Fig. 4). Nanoparticles show prominent concentration-dependency, wherein; 300 µg/mL concentration exhibited higher phenolic (145.81 ± 5.77 mg GAE/g dried weight) and flavonoid (72.35± 8.88 mg QE/g of dry weight) content compared to their 50 µg/mL concentration. Besides, quantitative estimation indicated that the percentage of antioxidant activity increased as the polyphenol compounds increased.

The shape and size of the Aw-Fe_3O_4 NPs were certified by the TEM image (Fig. 5a). The particle analysis of TEM images shows the spherical morphology with average size below 20 nm, which was accordant with the size (22 nm) calculated from the XRD results. Fig. S1 shows the SEM images of the Aw-Fe_3O_4 NPs. The dispersity of the Aw-Fe_3O_4 NPs in water was investigated by the dynamic light scattering (DLS), and the size of nanoparticles is 157 nm (Fig. S2). The size variation of the NPs using TEM and DLS can be relevant to the fundamental difference between the measurement method; in TEM analysis, distribution is based on the number of the particles while DLS measures the hydrodynamic size of NPs in the suspension and for polydisperse Aw-Fe_3O_4 NPs, these changes are more significant [67].

The surface area of the Aw-Fe_3O_4 NPs is a vital factor in adsorption experiments, which affects the behavior of an adsorbent. The nitrogen adsorption−desorption isotherm of Aw-Fe_3O_4 NPs at 77 K is shown in Fig. 5c. The Brunauer-Emmett-Teller (BET) surface area of Aw-Fe_3O_4 NPs is 32.63 m^2/g. This value is higher or similar to the other green synthesized Fe_3O_4 NPs reported in the

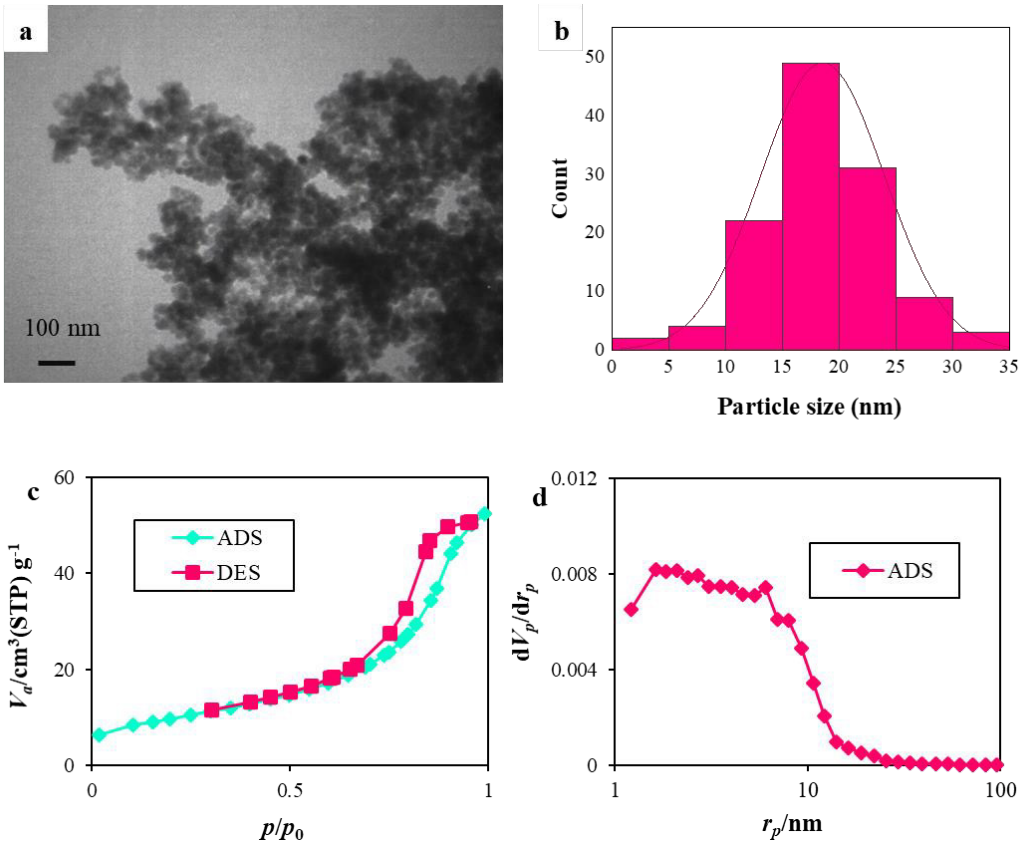

Fig. 5. Obtained microscopy data of Aw-Fe_3O_4 NPs: (a) TEM image; (b) Size distributions of particles, (c) N_2 adsorption-desorption isotherms of Aw-Fe_3O_4 NPs, (d) Pore size distributions calculated by the BJH method

literature [68].

The closed adsorption curve of the Aw-Fe_3O_4 NPs exhibits a type IV pattern in the high relative pressure (P/P_0) range of 0.5- 0.95, indicating the existence of mesoporous in Aw-Fe_3O_4 NPs. An H_1-type of the hysteresis loop, according to IUPAC classification, suggests that porous materials are consisting of cylindrical-like pores at both ends or agglomerates of approximately uniform spheres. The pore size distribution curve (Fig. 5d) evaluated by the Barret–Joyner and Halender's (BJH) method validates the mixture of the mesopore and macropore structure. It reveals that the Aw-Fe_3O_4 NPs sample contains large and small pores with an average pore diameter of 9.91 nm [69].

Adsorption studies

The prepared Aw-Fe_3O_4 NPs were applied for the adsorption of the MB dye. In the typical adsorption process, dyes were adsorbed on an adsorbent surface. Thus, the Aw-Fe_3O_4 NPs performance was highly dependent on its surface areas. To achieve maximum interaction of Aw-Fe_3O_4 with MB, selecting the optimum adsorbent dose is required. The experiments were done using 25, 50, 100, and 150 mg of Aw-Fe_3O_4 NPs in 35 mL of MB solutions (30 ppm) in a dark condition with continuous stirring. As shown in Fig. S4, the spectra of UV-visible absorption show a sharp peak at 665 nm, corresponding to the characteristic peak of MB. Fig. 6a provides a calibration curve of MB at different concentrations to calculate further MB concentration. Removal efficiency relies on the magnetite-dose illustrated in Fig. 6b. As Aw-Fe_3O_4 NPs doses increased, the MB removal increased as a result of the more active sites that available to bind dye. MB uptake rose from 35% to 69% as the dose went up from 25 to 100 mg, but did not significantly enhance at 150 mg (76%). Thus the 100 mg of Aw-Fe_3O_4 NPs was chosen as an

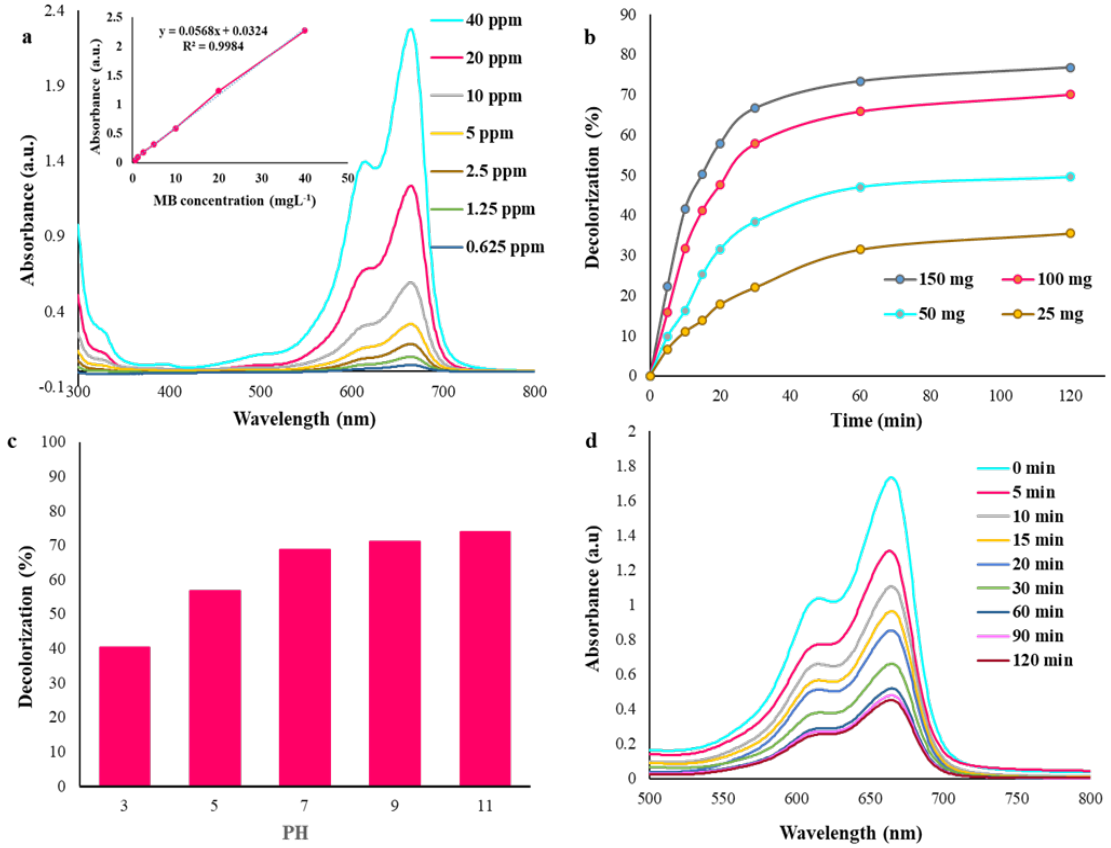

Fig. 6. (a) Calibration curve for MB absorbance in a range of 0.625–40 mgL^{-1}; (b) MB dye removal by different amount of Aw-Fe_3O_4 NPs at room temperature [[MB] = 30 mg/L, time = 120 min]; (c) Percentage MB dye removal at different initial solution pH [[MB] = 30 mg/L, [Aw-Fe_3O_4] =100 mg, time = 120 min]; (d) Successive UV–vis spectra of MB adsorption in the presence of Aw-Fe_3O_4 NPs samples at different time intervals [pH 11, [MB]= 30 mg/L, [Aw-Fe_3O_4] =100 mg].

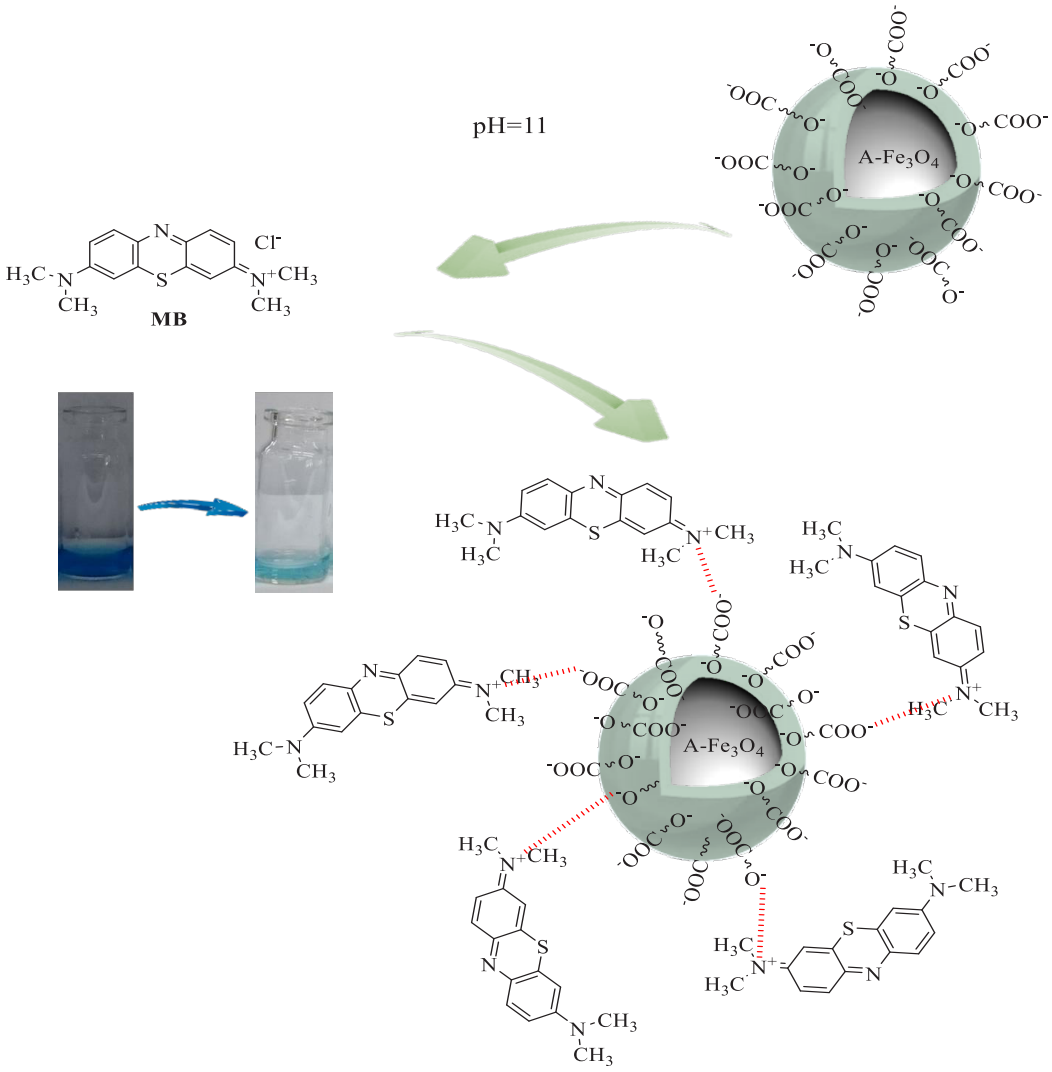

Fig. 7. Mechanism of MB adsorption onto Aw-Fe_3O_4 NPs.

optimum dose of the adsorbent. To investigate the roles of Aw in Aw-Fe_3O_4 NPs in removal efficiency of MB, the MB removal at the Aw-Fe_3O_4 NPs and chemical Fe_3O_4 NPs were investigated. The results indicated that the removal efficiency of MB was increased at the Aw-Fe_3O_4 NPs (removal efficiency increased about 1.67 times). Fig. S5 shows the UV-vis spectra of MB after exposure to Aw-Fe_3O_4 NPs at pH 11. The effect of pH on MB adsorption by Aw-Fe_3O_4 NPs is depicted in Fig. 6c. At pH 11, the maximum MB removal (73%) occurred due to electrostatic interaction between MB and magnetite. The adsorption substantially decreased as pH values were reduced from 11 to 5; removal reached 40%. This result is related to changes in the zeta potential of the Aw-Fe_3O_4 NPs at different pH values. The zeta potentials of the Aw-Fe_3O_4 NPs at pH 6, 8, and 10 are 17.5, -11.1, and -14.4, respectively, as demonstrated in Fig. S3. The zeta potential of the Aw-Fe_3O_4 NPs solution gradually changes from positive to negative when the pH value increases [70]. Therefore, carboxyl and hydroxyl groups on the surface of Aw-Fe_3O_4 NPs can protonate or deprotonate at the acidic or basic solution to generate ~OH_2^+ and ~$COOH_2^+$ or ~O^- and ~COO^- functional groups. Low adsorption occurred at acidic pH shows that the Aw-Fe_3O_4 NPs surfaces have positive charges [71]. According to the cationic nature of MB; repulsion forces are responsible for this effect. Possible mechanisms related to MB adsorption are demonstrated in Fig. 7. Thus, subsequent MB removal studies utilized

an optimum condition of 100 mg of Aw-Fe_3O_4 NPs at pH 11 (Fig. 6d).

Table S2 summarized the maximum adsorption capacity of Aw-Fe_3O_4 NPs compared to those reported in the literature for the adsorption of organic dye. It has been evident that the adsorption capacity of MB onto Aw-Fe_3O_4 NPs was higher than most of the already known green Fe_3O_4 reported in the literature. It is important to note that Aw-Fe_3O_4 NPs synthesis is more convenient, easier, and cheaper, without the use of any solvent for plant extraction in comparison with those existing green nanoparticles. However, the lack of calculation of the Fe_3O_4 maximum adsorption capacity in the literature has limited the comparison for us. It can be concluded the vital parameter such as total phenol and flavonoid, particle surface area, and size play an essential role in the absorption capacity.

Reusability of adsorbent

In an environmental application, reuse of the adsorbents is essential in terms of adsorbents' supply and economic standards; a regeneration study was done in acidic conditions to examine the adsorption capacity and stability of the Aw-Fe_3O_4 NPs after recovery. Regarding electrostatic interaction between MB and nanoparticles, acidic media can be utilized to release adsorbed MB. The possible reason for these results can be competition between H^+ and MB ions to the occupation of magnetite active-sites [72]. As illustrated in Fig. S6, the adsorption capacity of Aw-Fe_3O_4 NPs is still higher, with a slight decrease after the third cycle (69%). This small decrease in the recycling performance may be related to the loss of polyphenol compounds attached to the surface of Aw-Fe_3O_4 NPs. Hence, from the above results, the recovered Aw-Fe_3O_4 NPs can be used as a suitable adsorbent for MB removal.

MB dye adsorption kinetics studies

The adsorption kinetics data provide critical information about adsorption behaviors, including adsorption capacity, solute uptake rate, and chemical reaction. Fig. S7 demonstrates that the adsorption capacity of MB is affected by contact time with the Aw-Fe_3O_4 NPs. The adsorption capacity rose during the primary adsorption stage, then increased gradually with contact time and reached an equilibrium point after 60 min. To investigate the adsorption of MB onto the Aw-Fe_3O_4 NPs and to interpret the results, experimental data were fitted to the pseudo-first-order [72], the pseudo-second-order [73], and an intraparticle diffusion kinetic models [74]. The pseudo-first-order (Eq. (6)), pseudo-second-order kinetic model (Eq. (7)), and Weber's intraparticle diffusion model (Eq. (8)) are provided as the following equation:

$$\log(q_e - q_t) = \log q_e - \left(\frac{k_1}{2 \cdot 303}\right) t \quad (6)$$

$$\frac{t}{q_t} = \frac{1}{k_2 {q_e}^2} + \frac{t}{q_e} \quad (7)$$

$$q_t = k_i t^{\frac{1}{2}} + C \quad (8)$$

q_e, the adsorption capacity (mg/g) at equilibrium; q_t, the adsorption capacity (mg/g) at time t (min); k_1 (min^{-1}), the pseudo-first-order rate constant of adsorption; k_2 (g mg^{-1} min^{-1}), the pseudo-second-order rate constant; ki, the intraparticle diffusion rate constant (mg g^{-1} $min^{-1/2}$); C, the constant (mg/g) related to the thickness of the boundary layer.

The kinetic parameters obtained, as well as correlation coefficients (R^2) by linear regression, are summarized in Table 1. According to the results, the pseudo-second-order model is more applicable for explaining the adsorption data based on the higher correlation of coefficient (R^2) than that of the pseudo-first-order kinetics. Besides, the calculated q_e values of the pseudo-second-order kinetic model are close to the experimental ones ($q_{e,exp}$= 7.50). The pseudo-second-order kinetic model implies that the ionic exchange and chemisorption process are associated with the process of MB adsorption on Aw-Fe_3O_4 NPs. As shown in Fig. S8, the multi-linearity plot of the intraparticle diffusion model indicates two steps. Based on Weber and Morris's theory, the diffusion of MB molecules from the solution to the external surface of NPs occurred at the first stage and was finished at the second stage during the gradual diffusion of the dye molecules within the pores of the adsorbent. Thus, pseudo-second-order and intraparticle diffusion processes are performing MB adsorption onto Aw-Fe_3O_4 NPs [75].

CONCLUSION

In summary, iron oxide nanoparticles coated with Achillea wilhelmsii C. Koch extract with

the characteristics of easy separation were successfully prepared using a co-precipitation method. The prepared nanoparticles possessed great magnetism (~60), pure crystalline structure, and high adsorption capacity toward cationic dye like methylene blue (MB) (~8 mg/g). To evaluate the adsorption ability of Aw-Fe_3O_4 NPs as an adsorbent, MB was chosen as a model cationic dye. Adsorption tests show that MB was easier to adsorb on Aw-Fe_3O_4 NPs at high pH values, and maximum MB removal was observed at pH 11, although there was no significant difference was observed with pH 7. The phenolic compounds were deprotonated and revealed enhanced electrostatic interactions with high MB removal efficiency (73%). Moreover, the obtained nanoparticles showed efficient reusability after three cycles. The adsorption process was reasonably fitted with the pseudo-second-order and intraparticle diffusion kinetic model with high correlation coefficients. Overall, due to its low toxicity, efficiency, and suitable- reusable adsorption performance, Aw-Fe_3O_4 NPs can be considered as a promising candidate for commercial dye adsorption.

CONFLICT OF INTEREST

The authors declare that there is no conflict of interests regarding the publication of this manuscript.

REFERENCE

1. Majumder D, Chakraborty I, Mandal K, Roy S. Facet-Dependent Photodegradation of Methylene Blue Using Pristine CeO2 Nanostructures. ACS omega 2019;4(2):4243–4251.
2. Houas A, Lachheb H, Ksibi M, Elaloui E, Guillard C, Herrmann J-M. Photocatalytic degradation pathway of methylene blue in water. Appl Catal B Environ 2001;31(2):145–157.
3. Pooresmaeil M, Namazi H. Application of polysaccharide-based hydrogels for water treatments. In: Hydrogels based on natural polymers. Elsevier; 2020. page 411–455.
4. Katouli H, Khojasteh H, Golsefidi MA, Abbasi A, Ahmadi F, Rahimi-Nasrabadi M. Grafting of Ag nanoparticles on SrCrO 4 nanostructures: green synthesis, characterization, and photocatalytic study for organic dye degradation. J Mater Sci Mater Electron 2021;32(1):384–396.
5. Vinothkannan M, Karthikeyan C, Kim AR, Yoo DJ. One-pot green synthesis of reduced graphene oxide (RGO)/Fe_3O_4 nanocomposites and its catalytic activity toward methylene blue dye degradation. Spectrochim Acta Part A Mol Biomol Spectrosc 2015;136:256–264.
6. Narula A, Rao CP. Hydrogel of the Supramolecular Complex of Graphene Oxide and Sulfonatocalix [4] arene as Reusable Material for the Degradation of Organic Dyes: Demonstration of Adsorption and Degradation by Spectroscopy and Microscopy. ACS omega 2019;4(3):5731–5740.
7. Sobhani-Nasab A, Behvandi S, Karimi MA, Sohouli E, Karimi MS, Gholipour N, et al. Synergetic effect of graphene oxide and C3N4 as co-catalyst for enhanced photocatalytic performance of dyes on Yb2 $(MoO_4)_3$/$YbMoO_4$ nanocomposite. Ceram Int 2019;45(14):17847–17858.
8. Liu N, Wu Y. Removal of methylene blue by electrocoagulation: a study of the effect of operational parameters and mechanism. Ionics (Kiel) 2019;25(8):3953–3960.
9. Dafnopatidou EK, Lazaridis NK. Dyes removal from simulated and industrial textile effluents by dissolved-air and dispersed-air flotation techniques. Ind Eng Chem Res 2008;47(15):5594–5601.
10. Zamani A, Mahjoub AR, Seyed Sadjadi M. Synthesis and characterization of $MnFe_2O_4$@ ZnO-GO and $MnFe_2O_4$@ ZnO-rGO nanocomposites with evaluation of improved Photocatalytic performance Under Sun Light. J Nanostructures 2020;10(3):581–606.
11. Crini G, Lichtfouse E, Wilson LD, Morin-Crini N. Conventional and non-conventional adsorbents for wastewater treatment. Environ Chem Lett 2019;17(1):195–213.
12. Devi SM, Nivetha A, Prabha I. Superparamagnetic Properties and Significant Applications of Iron Oxide Nanoparticles for Astonishing Efficacy—a Review. J Supercond Nov Magn 2019;32(2):127–144.
13. Pooresmaeil M, Namazi H. pH-sensitive ternary Fe_3O_4/GQDs@ G hybrid microspheres; Synthesis, characterization and drug delivery application. J Alloys Compd 2020;846:156419.
14. Gandomi F, Sobhani-Nasab A, Pourmasoud S, Eghbali-Arani M, Rahimi-Nasrabadi M. Synthesis of novel Fe_3O_4@ SiO_2@ Er_2TiO_5 superparamagnetic core–shell and evaluation of their photocatalytic capacity. J Mater Sci Mater Electron 2020;31:10553–10563.
15. Attallah OA, Al-Ghobashy MA, Nebsen M, Salem MY. Removal of cationic and anionic dyes from aqueous solution with magnetite/pectin and magnetite/silica/pectin hybrid nanocomposites: kinetic, isotherm and mechanism analysis. RSC Adv 2016;6(14):11461–11480.
16. Pooresmaeil M, Mansoori Y, Mirzaeinejad M, Khodayari ALI. Efficient removal of methylene blue by novel magnetic hydrogel nanocomposites of poly (acrylic acid). Adv Polym Technol 2018;37(1):262–274.
17. Safari Z, Gholivand MB, Hosseinzadeh L. Spectrophotometric study of complex formations between 1-(2-pyridylazo)-2-naphthol (PAN) and some metal ions in organic solvents and the determination of thermodynamic parameters. Spectrochim Acta Part A Mol Biomol Spectrosc 2011;78(5):1606–1610.
18. Mazloum-Ardakani M, Maleki M, Khoshroo A. Synthesis of magnetic iron oxide nanoparticles and its application for simultaneous determination of hydrazine and hydroxylamine. J Nanostructures 2017;
19. Yadollahpour A. Magnetic nanoparticles in medicine: a review of synthesis methods and important characteristics. Orient J Chem 2015;31(Special Issue 1 (2015)):271–277.
20. Mazloum-Ardakani M, Khoshroo A, Hosseinzadeh L. Simultaneous determination of hydrazine and hydroxylamine based on fullerene-functionalized carbon nanotubes/ionic liquid nanocomposite. Sensors and Actuators B: Chemical. 2015;214:132-137.
21. Huang C, Zhang H, Sun Z, Zhao Y, Chen S, Tao R, et al.

Porous Fe_3O_4 nanoparticles: Synthesis and application in catalyzing epoxidation of styrene. J Colloid Interface Sci 2011;364(2):298–303.
22. Zhang J, Yao Y, Huang T, Yu A. Uniform hollow Fe_3O_4 spheres prepared by template-free solvothermal method as anode material for lithium-ion batteries. Electrochim Acta 2012;78:502–507.
23. Zhang W, Shen F, Hong R. Solvothermal synthesis of magnetic Fe_3O_4 microparticles via self-assembly of Fe_3O_4 nanoparticles. Particuology 2011;9(2):179–186.
24. Feng J, Mao J, Wen X, Tu M. Ultrasonic-assisted in situ synthesis and characterization of superparamagnetic Fe_3O_4 nanoparticles. J Alloys Compd 2011;509(37):9093–9097.
25. Cain JL, Harrison SR, Nikles JA, Nikles DE. Preparation of α-Fe particles by reduction of ferrous ion in lecithin/cyclohexane/water association colloids. J Magn Magn Mater 1996;155(1–3):67–79.
26. Demir A, Topkaya R, Baykal A. Green synthesis of superparamagnetic Fe_3O_4 nanoparticles with maltose: its magnetic investigation. Polyhedron 2013;65:282–287.
27. Sadegh H, Helmi H, Hamdy AS, Masjedi A, Dastjerdi MJH, Shahryari-ghoshekandi R. A developed simple, facile, economic and fast technique for preparation of high quality Fe_3O_4 magnetic nanoparticles. Chem Adv Mater 2016;1(1).
28. Khatami M, Alijani HQ, Fakheri B, Mobasseri MM, Heydarpour M, Farahani ZK, et al. Super-paramagnetic iron oxide nanoparticles (SPIONs): Greener synthesis using Stevia plant and evaluation of its antioxidant properties. J Clean Prod 2019;208:1171–1177.
29. Rasouli E, Basirun WJ, Rezayi M, Shameli K, Nourmohammadi E, Khandanlou R, et al. Ultrasmall superparamagnetic Fe_3O_4 nanoparticles: honey-based green and facile synthesis and in vitro viability assay. Int J Nanomedicine 2018;13:6903.
30. Bachheti RK, Konwarh R, Gupta V, Husen A, Joshi A. Green Synthesis of Iron Oxide Nanoparticles: Cutting Edge Technology and Multifaceted Applications. In: Nanomaterials and Plant Potential. Springer; 2019. page 239–259.
31. Yew YP, Shameli K, Miyake M, Khairudin NBBA, Mohamad SEB, Naiki T, et al. Green biosynthesis of superparamagnetic magnetite Fe_3O_4 nanoparticles and biomedical applications in targeted anticancer drug delivery system: A review. Arab J Chem 2018;
32. Kataria N, Garg VK. Green synthesis of Fe_3O_4 nanoparticles loaded sawdust carbon for cadmium (II) removal from water: regeneration and mechanism. Chemosphere 2018;208:818–828.
33. Bayat M, Beyki MH, Shemirani F. One-step and biogenic synthesis of magnetic Fe_3O_4–Fir sawdust composite: Application for selective preconcentration and determination of gold ions. J Ind Eng Chem 2015;21:912–9.
34. Nnadozie EC, Ajibade PA. Green synthesis and characterization of magnetite (Fe_3O_4) nanoparticles using Chromolaena odorata root extract for smart nanocomposite. Mater Lett 2020;263:127145.
35. Singh KK, Senapati KK, Sarma KC. Synthesis of superparamagnetic Fe_3O_4 nanoparticles coated with green tea polyphenols and their use for removal of dye pollutant from aqueous solution. J Environ Chem Eng 2017;5(3):2214–2221.
36. Prasad C, Karlapudi S, Venkateswarlu P, Bahadur I, Kumar S. Green arbitrated synthesis of Fe_3O_4 magnetic nanoparticles with nanorod structure from pomegranate leaves and Congo red dye degradation studies for water treatment. J Mol Liq 2017;240:322–328.
37. Patra JK, Baek K-H. Green biosynthesis of magnetic iron oxide (Fe_3O_4) nanoparticles using the aqueous extracts of food processing wastes under photo-catalyzed condition and investigation of their antimicrobial and antioxidant activity. J Photochem Photobiol B Biol 2017;173:291–300.
38. Ashtiani M, Nabatchian F, Galavi HR, Saravani R, Farajian-Mashhadi F, Salimi S. Effect of Achillea wilhelmsii extract on expression of the human telomerase reverse transcriptase mRNA in the PC3 prostate cancer cell line. Biomed reports 2017;7(3):251–256.
39. Niazmand S, Khoshnood E. The effects of Achillea wilhelmsii extract on Rat's gastric motility at basal and vagal stimulated conditions. Iran J Basic Med Sci 2011;14(2):151–157.
40. Khazneh E, Hřibová P, Hošek J, Suchý P, Kollár P, Pražanová G, et al. The chemical composition of Achillea wilhelmsii C. Koch and its desirable effects on hyperglycemia, inflammatory mediators and hypercholesterolemia as risk factors for cardiometabolic disease. Molecules 2016;21(4):404.
41. Gironi F, Piemonte V. Temperature and solvent effects on polyphenol extraction process from chestnut tree wood. Chem Eng Res Des 2011;89(7):857–862.
42. Sentkowska A, Biesaga M, Pyrzynska K. Polyphenolic composition and antioxidative properties of lemon balm (Melissa officinalis L.) extract affected by different brewing processes. Int J Food Prop 2015;18(9):2009–2014.
43. Ovais M, Khalil AT, Islam NU, Ahmad I, Ayaz M, Saravanan M, et al. Role of plant phytochemicals and microbial enzymes in biosynthesis of metallic nanoparticles. Appl Microbiol Biotechnol 2018;102(16):6799–6814.
44. Amjad L, Mohammadi-Sichani M, Mohammadi-Kamalabadi M. Potential activity of the Achillea wilhelmsii leaves on bacteria. Int J Biosci Biochem Bioinforma 2011;1(3):216.
45. Amjad L, Mousavidehmourdi K, Saghazadeh M. Antifungal potential of Achillea wilhelmsii flowers methanolic extract on different strains of Candida albicans. Int J Biol Med Res 2012;3(3):2107–2110.
46. Ainsworth EA, Gillespie KM. Estimation of total phenolic content and other oxidation substrates in plant tissues using Folin–Ciocalteu reagent. Nat Protoc 2007;2(4):875–887.
47. Asariha M, Chahardoli A, Karimi N, Gholamhosseinpour M, Khoshroo A, Nemati H, et al. Green synthesis and structural characterization of gold nanoparticles from Achillea wilhelmsii leaf infusion and in vitro evaluation. Bull Mater Sci 2020;43(1):57.
48. Mavaei M, Chahardoli A, Shokoohinia Y, Khoshroo A, Fattahi A. one-step Synthesized Silver nanoparticles Using isoimperatorin: evaluation of photocatalytic, and electrochemical Activities. Sci Rep 2020;10(1):1–12.
49. Jalilian F, Chahardoli A, Sadrjavadi K, Fattahi A, Shokoohinia Y. Green synthesized silver nanoparticle from Allium ampeloprasum aqueous extract: Characterization, antioxidant activities, antibacterial and cytotoxicity effects. Adv Powder Technol 2020;
50. Ahmed S, Ahmad M, Swami BL, Ikram S. A review on plants extract mediated synthesis of silver nanoparticles for antimicrobial applications: a green expertise. J Adv Res 2016;7(1):17–28.
51. Darvishi E, Kahrizi D, Arkan E. Comparison of different properties of zinc oxide nanoparticles synthesized by the green (using Juglans regia L. leaf extract) and chemical

methods. J Mol Liq 2019;286:110831.
52. Jafari M, Naeini KM, Lorigooini Z, Namjoo R. Oral acute and sub-acute toxic effects of hydroalcoholic Terminalia chebula Retz and Achillea wilhelmsii extracts in BALB/c mice. BioMedicine 2019;9(4).
53. ŞABANOĞLU S, GÖKBULUT A, ALTUN ML. Characterization of phenolic compounds, total phenolic content and antioxidant activity of three Achillea species. Marmara Pharm J 2019;23(3).
54. Mishra PM, Naik GK, Nayak A, Parida KM. Facile synthesis of nano-structured magnetite in presence of natural surfactant for enhanced photocatalytic activity for water decomposition and Cr (VI) reduction. Chem Eng J 2016;299:227–235.
55. Schwertmann U, Friedl J, Stanjek H. From Fe (III) ions to ferrihydrite and then to hematite. J Colloid Interface Sci 1999;209(1):215–223.
56. Rajput S, Pittman Jr CU, Mohan D. Magnetic magnetite (Fe_3O_4) nanoparticle synthesis and applications for lead (Pb^{2+}) and chromium (Cr^{6+}) removal from water. J Colloid Interface Sci 2016;468:334–346.
57. Gnanaprakash G, Mahadevan S, Jayakumar T, Kalyanasundaram P, Philip J, Raj B. Effect of initial pH and temperature of iron salt solutions on formation of magnetite nanoparticles. Mater Chem Phys 2007;103(1):168–75.
58. Nasrollahzadeh M, Atarod M, Sajadi SM. Green synthesis of the Cu/Fe_3O_4 nanoparticles using Morinda morindoides leaf aqueous extract: a highly efficient magnetically separable catalyst for the reduction of organic dyes in aqueous medium at room temperature. Appl Surf Sci 2016;364:636–644.
59. Mabry TJ, Markham KR, Thomas MB. The ultraviolet spectra of flavones and flavonols. In: The systematic identification of flavonoids. Springer; 1970. page 41–164.
60. Michira IN, Katithi DN, Guto P, Kamau GN, Baker P, Iwuoha E. Synthesis, characterization of green tea stabilized iron nanoparticles and their synergistic effect on polyaniline. Int J Sci Basic Appl Res 2014;13(2).
61. Chahrdoli A, Qalekhani F, Ghowsi M, Nemati H, Shokoohinia Y, Fattahi A. Achillea wilhelmsii C. Koch mediated blood compatible silver nanoparticles. Mater Today Commun 2020;25:101577.
62. Xiao L, Mertens M, Wortmann L, Kremer S, Valldor M, Lammers T, et al. Enhanced in vitro and in vivo cellular imaging with green tea coated water-soluble iron oxide nanocrystals. ACS Appl Mater Interfaces 2015;7(12):6530–6540.
63. Jiang W, Lai K, Liu K, Xia R, Gao F, Wu Y, et al. "Green" functionalization of magnetic nanoparticles via tea polyphenol for magnetic resonance/fluorescent dual-imaging. Nanoscale 2014;6(3):1305–1310.
64. Roca AG, Morales MP, Serna CJ. Synthesis of monodispersed magnetite particles from different organometallic precursors. Ieee Trans Magn 2006;42(10):3025–3029.
65. Li W, Liu D, Wu J, Kim C, Fortner JD. Aqueous aggregation and surface deposition processes of engineered superparamagnetic iron oxide nanoparticles for environmental applications. Environ Sci Technol 2014;48(20):11892–11900.
66. Dorniani D, Hussein MZ Bin, Kura AU, Fakurazi S, Shaari AH, Ahmad Z. Preparation of Fe_3O_4 magnetic nanoparticles coated with gallic acid for drug delivery. Int J Nanomedicine 2012;7:5745.
67. Kaasalainen M, Aseyev V, von Haartman E, Karaman DŞ, Mäkilä E, Tenhu H, et al. Size, stability, and porosity of mesoporous nanoparticles characterized with light scattering. Nanoscale Res Lett 2017;12(1):74.
68. Cheera P, Karlapudi S, Sellola G, Ponneri V. A facile green synthesis of spherical Fe_3O_4 magnetic nanoparticles and their effect on degradation of methylene blue in aqueous solution. J Mol Liq 2016;221:993–938.
69. Azari A, Gharibi H, Kakavandi B, Ghanizadeh G, Javid A, Mahvi AH, et al. Magnetic adsorption separation process: an alternative method of mercury extracting from aqueous solution using modified chitosan coated Fe_3O_4 nanocomposites. J Chem Technol Biotechnol 2017;92(1):188–200.
70. Feng L, Cao M, Ma X, Zhu Y, Hu C. Superparamagnetic high-surface-area Fe_3O_4 nanoparticles as adsorbents for arsenic removal. J Hazard Mater 2012;217:439–446.
71. Jawad AH, Abdulhameed AS. Mesoporous Iraqi red kaolin clay as an efficient adsorbent for methylene blue dye: Adsorption kinetic, isotherm and mechanism study. Surfaces and Interfaces 2020;18:100422.
72. Abdallah R, Taha S. Biosorption of methylene blue from aqueous solution by nonviable Aspergillus fumigatus. Chem Eng J 2012;195:69–76.
73. Ho Y-S, McKay G. Pseudo-second order model for sorption processes. Process Biochem 1999;34(5):451–65.
74. Weber WJ, Morris JC. Kinetics of adsorption on carbon from solution. J Sanit Eng Div 1963;89(2):31–60.
75. Ai L, Zhang C, Liao F, Wang Y, Li M, Meng L, et al. Removal of methylene blue from aqueous solution with magnetite loaded multi-wall carbon nanotube: kinetic, isotherm and mechanism analysis. J Hazard Mater 2011;198:282–290.